energies

MDPI

Article

Mechanistic Model of an Air Cushion Surge Tank for Hydro Power Plants

Madhusudhan Pandey [1], Dietmar Winkler [1], Kaspar Vereide [2], Roshan Sharma [1] and Bernt Lie [1,*]

[1] Telemark Modeling and Control Center (TMCC), University of South-Eastern Norway (USN), 3918 Porsgrunn, Norway; madhusudhan.pandey@usn.no (M.P.); dietmar.winkler@usn.no (D.W.); roshan.sharma@usn.no (R.S.)

[2] Department of Civil and Environmental Engineering, Norwegian University of Science and Technology, 7034 Trondheim, Norway; kaspar.vereide@ntnu.no

* Correspondence: bernt.lie@usn.no

Abstract: Due to the increasing use of renewable energy sources, and to counter the effects of fossil fuels, renewable dispatchable hydro power can be used for balancing load and generation from intermittent sources (solar and wind). During higher percentage change in load acceptance or rejection in the intermittent grid, the operations of surge tanks are crucial in terms of water mass oscillation and water hammer pressure, and to avoid wear and tear in actuators and other equipment, such as hydro turbines. Surge tanks are broadly classified as open types, with access to open air, and closed types, with a closed volume of pressurized air. Closed surge tanks are considered to have a more flexible operation in terms of suppressing water mass oscillation and water hammer pressure. In this paper, a mechanistic model of an air cushion surge tank (ACST) for hydro power plants is developed based on the ordinary differential equations (ODEs) for mass and momentum balances. The developed mechanistic model of the ACST is a feature extension to an existing open-source hydro power library—OpenHPL. The developed model is validated with experimental data from the Torpa hydro power plant (HPP) in Norway. Results show that the air friction inside the ACST is negligible as compared to the water friction. The results also indicate that a hydro power plant with an ACST is a potential candidate as a flexible hydro power in an interconnected power system grid supplied with intermittent energy sources. Conclusions are drawn based on the simulation results from hydraulic performance of the ACST.

Keywords: air cushion surge tank (ACST); air friction model; flexible hydro power plants; mechanistic model; OpenHPL

Citation: Pandey, M.; Winkler, D.; Vereide, K.; Sharma, R.; Lie, B. Mechanistic Model of an Air Cushion Surge Tank for Hydro Power Plants. *Energies* **2022**, *15*, 2824. https://doi.org/10.3390/en15082824

Academic Editors: Adam Adamkowski and Anton Bergant

Received: 17 March 2022
Accepted: 11 April 2022
Published: 13 April 2022

1. Introduction

1.1. Background

Electricity generation from renewable energy is increasing because of oil insecurity, climatic concern, the nuclear power debate, and carbon emission prices. In a growing trend of renewable energy, today's power systems are a combination of intermittent and dispatchable renewable sources in a common interconnected grid. Intermittent sources include sources like solar power plants and wind power plants, whose variability can be balanced using a dispatchable renewable source like a hydro power plant, as discussed in [1,2]. In an interconnected power grid with both intermittent and dispatchable sources, a sudden loss in generation from the intermittent sources, for example, shadowing a large number of solar panels as in the case of solar power plants, a shutdown of the wind generators for unacceptable wind velocity as in the case of wind power plants, hydro power plants must be able to operate with a higher percentage of load acceptance to cope with the loss in generation, and to protect the power grid from a blackout. Similarly, when there is a sudden increase in production from the intermittent generation, hydro power plants must be able to operate with a higher percentage of load rejection to cope with grid

instability and blackout. This indicates the need for flexible operation of dispatchable hydro power plants. In [3,4], the concept of *flexible hydro power* is coined for the interconnected power grid. Similarly, in [5] cascaded hydro power plants are considered as one of the candidates for flexible hydro power plants. In relation to the concept of flexible hydro power, hydro power plants with open surge tanks are relatively less able to tackle a higher percentage of load acceptance and rejection. However, power plants with ACST are more likely to tackle a higher percentage of load acceptance and rejection as ACST can be placed very near to the turbine. Hydraulic behavior of the open surge tanks studied in [6] outlines their operational limits in terms of their design heights and water hammer effects. As the percentage of load acceptance and rejection increases in the case of the open surge tanks, water mass oscillation inside the surge tanks may exceed the maximum allowed height and the operational limit of the power plant equipment due to an excessive water hammer effect. Similarly, in [7,8] the benefits of ACST with respect to open surge tanks are given.

In this regard, it is of interest to study the hydraulic behavior of an ACST (closed surge tank) with respect to open surge tanks. A simple mechanistic model of an ACST was developed and studied previously in [9] as a feature extension to an open-source hydro power library—OpenHPL. OpenHPL is based on an equation-based language—Modelica. OpenHPL is under development at the University of South-Eastern Norway. This paper primarily focuses on the model improvements from [9], validation of the improved model with experimental data from [10], and hydraulic behavior of an ACST in relation to flexible hydro power plants.

1.2. Previous Work and Contributions

The model of hydraulic transients inside the surge tank is a well-established theory using Newton's second law [11,12]. The use of hydraulic resistances in the inlet of the surge tank helps to reduce water hammer effects. Different types of surge tanks designed with respect to the hydraulic resistances are presented in [13]. The time evolution equations for developing a mechanistic model of the surge tank are given in [14]. The hydraulic resistance at the inlet of different kinds of surge tanks can be studied from [14,15]. Closed surge tanks or ACST are important in terms of suppressing water mass oscillation due to the cushioning of air during hydraulic transients [16]. A hydraulic scale model of an ACST was studied in [10] based on 1D mass and momentum balances. In [17], a simulation study was carried out considering 1D mass and momentum equations for both water and air inside the ACST. In the paper, it is shown that the mass and momentum balances for air inside the ACST can be further simplified with an ideal gas relation. Other studies include the gas seepage theory for air loss through the ACST chamber in [18], a monitoring method for the hydraulic behavior of the ACST in [19], stability analysis of the ACST in [20], etc. The model developed in most of the previous work assumes an adiabatic process for the cushioning of air inside the ACST. The polytropic constant for air γ is considered around 1.4 for almost all the models of the ACST. However, previous work lacks modeling of the ACST with a possible consideration of friction due to air flow inside the ACST during its operation. The following research contributions are provided in this paper:

- a mechanistic model of an ACST, and
- a comparison between the ACST models with and without air friction.

1.3. Outline

Section 2 provides a mechanistic model of an ACST based on mass and momentum balances. In Section 3, model fitting and simulation results are outlined through a case study of the ACST used in Torpa Hydro Power Plant (HPP). Section 4 provides conclusions and future work.

2. Mechanistic Model of ACST

A general schematic and a flow diagram of an ACST is shown in Figure 1. The free water surface inside the surge tank is filled with pressurized air. Figure 1a shows the general

schematic of an ACST where the water with volumetric flow rate $\dot{V}$ flows towards the air chamber through the access tunnel with length L_t and diameter D_t. The intake-penstock manifold pressure at the bottom of the tank is represented by p_m, and the air pressure at the air chamber due to the cushioning of the air is represented by p_c. The diameter of the air chamber is D. H is the total height of the surge tank and L is the total vertical slant length of the surge tank. In the figure, h represents the water level inside the tank during the operation of the ACST, and the dotted line in Figure 1a indicates that h is a variable quantity. Figure 1b shows a flow diagram inside the surge tank where F_f is the fluid friction against $\dot{V}$, F_g is the force due to gravity in the downward direction, and $F_g^{\dot{V}}$ is the projection of F_g in the alignment of the flow.

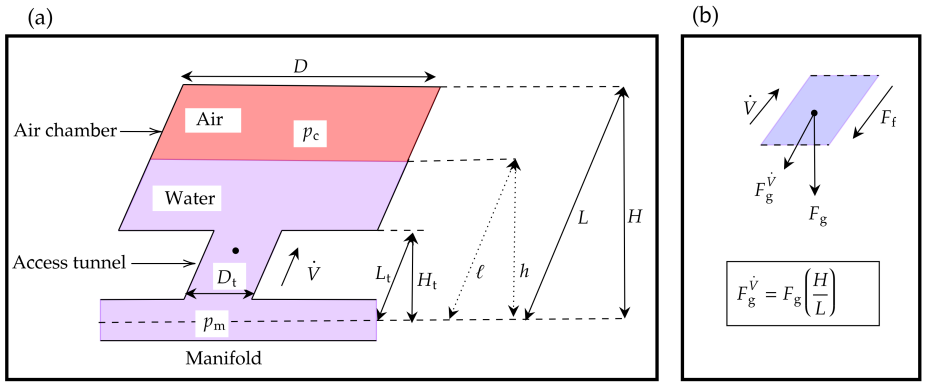

Figure 1. ACST with an access tunnel and an air chamber. (**a**) general schematic of ACST and (**b**) flow diagram.

Models developed in OpenHPL are based on a semi-explicit DAE formulation with a differential equation for the mass and the momentum balances as described in [21] and given by

$$\frac{dm}{dt} = \dot{m} \tag{1}$$

$$\frac{d\mathcal{M}}{dt} = \dot{\mathcal{M}} + F \tag{2}$$

where $\dot{m}$ and $\dot{\mathcal{M}}$ represent the mass flow rate and the momentum flow rate, respectively.

Equations (1) and (2) are expressed with a series of algebraic equations as

$$\dot{m} = \rho \dot{V} \tag{3}$$

$$\mathcal{M} = mv \tag{4}$$

$$\dot{\mathcal{M}} = \dot{m}v \tag{5}$$

$$F = F_p - F_g^{\dot{V}} - F_f \tag{6}$$

where ρ is the density of the water, m is the mass of air and water inside the ACST, v is the average velocity of the flow, V is the volume of the ACST, F is the total force acting in the surge tank, F_p is the pressure force, and F_f is the fluid frictional force. The expressions for all the variables are given in the sequel. A general idea regarding mathematical formulations of these variables is taken from [9].

The total mass inside the surge tank is expressed as

$$m = m_w + m_a \tag{7}$$

where m_w and m_a are the masses of the water and the air inside the surge tank, respectively. m_a is constant inside the chamber and is determined based on the initial air cushion pressure p_{c0} which is considered to be a design parameter for the hydraulic performance

of the surge tank. If h_{c0} is the initial water level inside the surge tank for the initial air cushion pressure p_{c0}, then the expression for the mass of the air inside the surge tank is found from an adiabatic compression and rarefaction of the air inside the surge tank during operation. It is found that for an ACST with a larger diameter, the heat transfer between air and water, air to the walls of the ACST, etc., can be neglected, and an adiabatic process of compression and rarefaction of the air inside the ACST can be assumed [16]. For an adiabatic process with pressure p, volume V, and γ of the air inside the ACST, considering standard temperature and pressure (STP), the relation $pV^{\gamma} =$ constant is assumed where γ is the ratio of specific heats at constant pressure and at constant volume. The mass of the air is then calculated formulating an ideal gas relation with the initial air pressure p_{c0} and the initial volume $A\left(L - h_{c0}\frac{L}{H}\right)$ given by

$$m_a = \frac{p_{c0}A\left(L - h_{c0}\frac{L}{H}\right)M_a}{RT^{\circ}} \tag{8}$$

where M_a is the molar mass of air, R is the universal gas constant and T° is the temperature taken at STP. Similarly, A is the area of the air chamber expressed as $A = \pi\frac{D^2}{4}$.

From Equation (2) formulating $p_{c0}V_0^{\gamma} = p_c V^{\gamma}$, the air cushion pressure during the operation of the surge tank is given by

$$p_c = p_{c0}\left(\frac{L - h_{c0}\frac{L}{H}}{L - \ell}\right)^{\gamma} \tag{9}$$

where p_c depends on the length ℓ inside the ACST.

During the operation of the surge tank, the mass of the water inside the surge tank m_w varies according to the variation in h. Thus, the expression for m_w is formulated considering two different scenarios inside the surge tank based on the variation of the water level h. First we consider (i) $h \leq H_t$ and second we consider (ii) $h > H_t$. Furthermore, we also formulate expressions for F_p and F_f for both of the scenarios of the water level h.

2.1. Case $h \leq H_t$

When the water level is up to the tip of the access tunnel or below the tip of the access tunnel, m_w is given by $m_w = \rho A_t \ell$ where ℓ is the slant height for h as shown in Figure 1a. m_w is further expressed as

$$m_w = \rho A_t h\frac{L}{H}. \tag{10}$$

The pressure force F_p is formulated based on the pressure difference at the manifold and the air pressure with an expression

$$F_p = (p_m - p_c)A_t. \tag{11}$$

The frictional force F_f is expressed as

$$F_f = F_{D,w} + F_{D,a} \tag{12}$$

where $F_{D,w}$ is the frictional force formulated for water flow inside the surge tank based on Darcy's friction factor for water, $f_{D,w}$. Similarly, $F_{D,a}$ is the frictional force formulated for air flow inside the surge tank based on Darcy's friction factor for air, $f_{D,a}$. Both $f_{D,w}$ and $f_{D,a}$ are calculated as in [9]. The general expression for Darcy's friction factor f_D is based on Reynolds' number $N_{Re} = \frac{\rho|v|D}{\mu}$ and expressed as

$$f_D = \begin{cases} \frac{64}{N_{\mathrm{Re}}} & N_{\mathrm{Re}} < 2100 \\ aN_{\mathrm{Re}}^3 + bN_{\mathrm{Re}}^2 + cN_{\mathrm{Re}} + d & 2100 \le N_{\mathrm{Re}} \le 2300 \\ \frac{1}{\left(2\log_{10}\left(\frac{\varepsilon}{3.7D} + \frac{5.7}{N_{\mathrm{Re}}^{0.9}}\right)\right)^2} & N_{\mathrm{Re}} > 2300 \end{cases}$$

where μ is the dynamic viscosity of the fluid, ε is the pipe roughness height. For the region $2100 \le N_{\mathrm{Re}} \le 2300$, f_{D} is calculated from a cubic interpolation, with the coefficients a, b, c, and d, differentiable at the boundaries. The final expression for F_{f} is calculated as in [9] given as

$$F_{\mathrm{f}} = \frac{1}{2}\rho v \mid v \mid \left(A_{\mathrm{w,w}}\frac{f_{\mathrm{D,w}}}{4} + A_{\mathrm{w,a}}\frac{f_{\mathrm{D,a}}}{4}\right) \tag{13}$$

where $\mid v \mid$ preserves the fluid frictional force against both directions of flow; flow induced from the access tunnel towards the air chamber, and vice-versa. $A_{\mathrm{w,w}}$ is the wetted area due to water flow inside the surge tank given by

$$A_{\mathrm{w,w}} = \pi D_{\mathrm{t}} \ell \tag{14}$$

and $A_{\mathrm{w,a}}$ is the wetted area due to the air during adiabatic compression and rarefaction inside the surge tank, and expressed as

$$A_{\mathrm{w,a}} = \pi[D(L - L_{\mathrm{t}}) + D_{\mathrm{t}}(L_{\mathrm{t}} - \ell)]. \tag{15}$$

2.2. Case $h > H_{\mathrm{t}}$

When the water level inside the surge tank is above the access tunnel expression for m_{w} is formulated by summing the mass of water inside the access tunnel and the mass of water inside the air chamber, and is expressed as

$$m_{\mathrm{w}} = \rho[A_{\mathrm{t}}L_{\mathrm{t}} + A(\ell - L_{\mathrm{t}})]. \tag{16}$$

For $\ell > L_{\mathrm{t}}$ we consider Figure 2 for finding the total pressure force F_{p} in the direction of the flow. The calculation of the fluid frictional force is given in Figure 3. From Figure 2, the pressure force F_{p} is calculated based on the junction pressure p_{j} between the junction of the access tunnel and the air chamber. p_{j} is expressed as the sum of the air pressure p_{c} and the hydrostatic pressure due to the difference in liquid-level $h - H_{\mathrm{t}}$. The junction pressure is then expressed as

$$p_{\mathrm{j}} = p_{\mathrm{c}} + \rho g(\ell - L_{\mathrm{t}})\frac{H}{L} \tag{17}$$

which relates in the final expression for F_{f} as

$$F_{\mathrm{p}} = (p_{\mathrm{m}} - p_{\mathrm{j}})A_{\mathrm{t}} + (p_{\mathrm{j}} - p_{\mathrm{c}})A. \tag{18}$$

From Figure 2, the overall fluid frictional force F_{f} is calculated with an expression given as

$$F_{\mathrm{f}} = F_{\mathrm{D,w}} + F_{\phi} + F_{\mathrm{D,a}} \tag{19}$$

where $F_{\mathrm{D,w}} + F_{\mathrm{D,a}}$ is given as

$$F_{\mathrm{D,w}} + F_{\mathrm{D,a}} = \frac{1}{2}\rho v \mid v \mid \left(A_{\mathrm{w,w}}\frac{f_{\mathrm{D,w}}}{4} + A_{\mathrm{w,a}}\frac{f_{\mathrm{D,a}}}{4}\right)$$

where $A_{\mathrm{w,w}} = \pi[D_{\mathrm{t}}L_{\mathrm{t}} + D(\ell - L_{\mathrm{t}})]$ and $A_{\mathrm{w,a}} = \pi D(L - \ell)$; the calculations were similarly performed as in Equations (14) and (15).

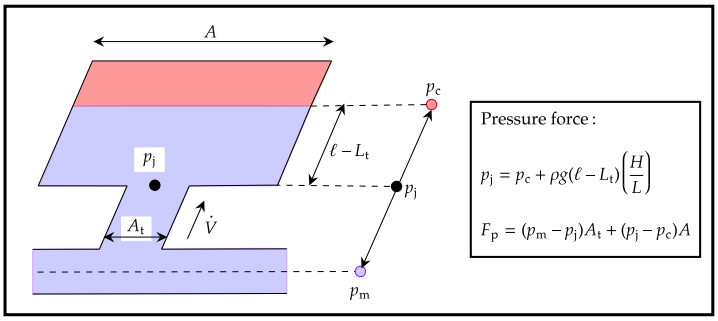

Figure 2. Considering junction pressure p_j for evaluating the overall pressure force F_p in the direction of flow. p_j is the pressure calculated based on the sum of air pressure p_c and hydrostatic pressure due to liquid-level $h - H_t$.

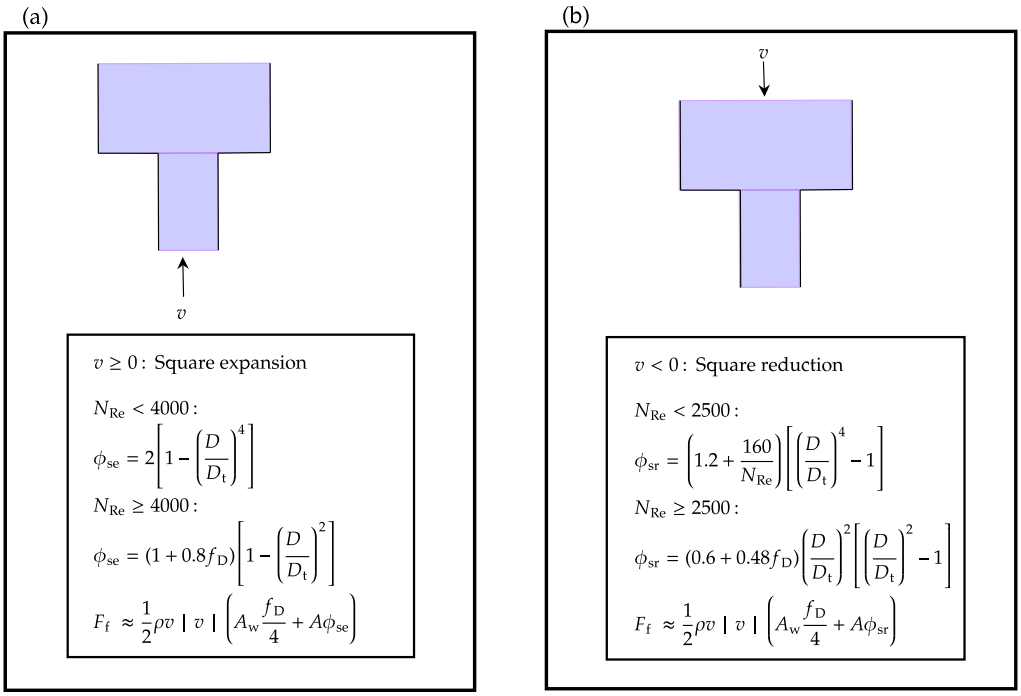

Figure 3. Expressions for fluid frictional force F_f considering (**a**) the square expansion type fitting for the flow towards the chamber through the access tunnel and (**b**) the square reduction type fitting for the flow through the chamber to the access tunnel. In the figures, ϕ_{se} and ϕ_{sr} are the generalized friction factors for the square expansion and the square reduction type fittings, respectively, taken from [15].

In Equation (19), F_ϕ is the fluid frictional force due to water flow from the access tunnel towards the air chamber, and vice-versa. F_ϕ can be expressed in terms of the pressure drop (alternatively can be expressed in terms of the head loss). When the water is flowing *from the access tunnel towards the air chamber*, we consider the pressure drop due to the *square expansion* type of fitting as shown in Figure 3a, and when the water is flowing *from the air chamber towards the access tunnel*, we consider the pressure drop due to the *square reduction* type of fitting as shown in Figure 3b. Thus, F_ϕ is calculated based on the generalized friction factors ϕ_{se} for the square expansion type of fitting and ϕ_{sr} for the square reduction type of fitting. Additionally, for both types of flows as shown in Figure 3, we assume an average cross-sectional area

$$\bar{A} = \frac{A + A_t}{2}.$$

If Δp_ϕ is the pressure drop due to the fittings, there exists a relationship between Δp_ϕ, the average kinetic energy of the fluid per volume $K''' = \frac{1}{2}\rho v \mid v \mid$ and the friction factor $\phi = \{\phi_{\text{se}}, \phi_{\text{sr}}\}$. The relationship between Δp_ϕ, K''', and ϕ is given by

$$\Delta p_\phi = \phi K'''.$$

The pressure drop Δp_ϕ is related to F_ϕ through the average cross-sectional area $\bar{A}$ and given as

$$F_\phi \approx \Delta p_\phi \bar{A}$$

which can be further expressed as

$$F_\phi \approx \frac{1}{2}\rho v \mid v \mid \bar{A}\phi, \quad \phi = \{\phi_{\text{se}}, \phi_{\text{sr}}\}.$$

The final expression for overall fluid frictional force F_{f} is then given as

$$F_{\text{f}} \approx \frac{1}{2}\rho v \mid v \mid \left(A_{\text{w,w}} \frac{f_{\text{D,w}}}{4} + A_{\text{w,a}} \frac{f_{\text{D,a}}}{4} + \bar{A}\phi \right) \quad \phi = \{\phi_{\text{se}}, \phi_{\text{sr}}\}. \tag{20}$$

This completes the expressions for variables m, F_{p} and F_{f} for the two scenarios of the liquid level inside the surge tank, viz., $h \leq H_{\text{t}}$ and $h > H_{\text{t}}$. To further complete the information of variables in Equation (6), the expression for $F_{\text{g}}^{\dot{V}}$ is calculated as

$$F_{\text{g}}^{\dot{V}} = mg\frac{H}{L}, \tag{21}$$

as shown in the flow diagram of Figure 1a. Finally, the mechanistic model of the ACST needs an expression for the average velocity v expressed as

$$v = \frac{\dot{V}}{\bar{A}}. \tag{22}$$

Equations (1)–(6), in addition to other associated algebraic relations from Equations (7)–(22), represent a semi-explicit DAEs formulation for the ACST, and can be modeled in a equation-based modeling language like Modelica. The developed mechanistic model of the ACST is implemented in OpenHPL as a feature extension, and the case study was carried out for Torpa HPP.

3. Case Study

Figure 4a shows the layout diagram of Torpa HPP. Similarly, Figure 4b shows the simulation model of Torpa HPP created in OpenHPL. In Figure 4b, the reservoir model, the intake tunnel model, the penstock model, and the discharge model are developed as in [21]. A detailed model of the penstock considering water compressibility and pipe elasticity can be formulated from [22]. However, we consider the penstock model as a simple pipe model. Similarly, the Francis turbine mechanistic model for the case study is modeled as in [23]. The mechanistic model for the tailrace is taken as an exact mirror replica of the reservoir model.

The dimensions of the ACST shown in Figure 4a are found based on the piezometric diagram for Torpa HPP from [10]. The model developed in Section 2 is based on a cylindrical access tunnel and a cylindrical air chamber. Thus, the hydraulic diameters for the access tunnel D_{t} and the air chamber D are evaluated based on the volume of air inside the chamber using the operating conditions. Table 1 shows the parameters and the operating conditions of the ACST for Torpa HPP.

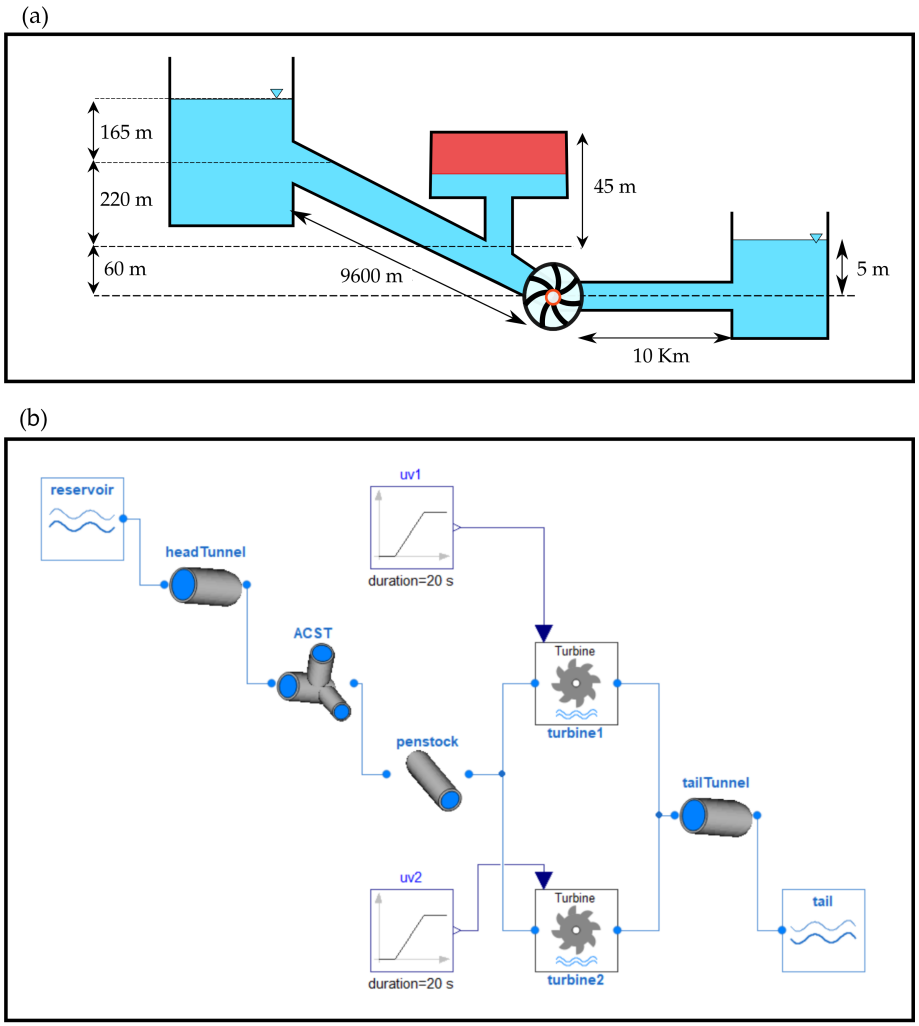

Figure 4. (**a**) Layout diagram for Torpa HPP. Nominal head, nominal discharge, and nominal power output are 445 m, 40 m^3/s and 150 MW, respectively. The ACST has air volume of 13,000 m^3, initially pressurized at $41 \cdot 10^5$ Pa. Similarly, both of the headrace and tailrace tunnels are 7 m in diameter. Torpa HPP consists of two turbine units each rated at 75 MW with rated discharge at 20 m^3/s. Torpa HPP also consists of a tailrace surge tank not shown in the figure. (**b**) Simulation model of Torpa HPP implemented in OpenHPL from the head reservoir to the tail reservoir.

For the model created in Figure 4b, it is of interest to:

1. validate the model with the experimental data from [10],
2. simulate the model considering air friction inside the ACST, and
3. study the hydraulic behavior of the ACST at different load acceptances and rejections.

3.1. Simulation Versus Real Measurements

Figure 5 shows the simulated versus real measurement for Torpa HPP. As shown in Figure 4b, u_{v1} and u_{v2} are the turbine valve signals for the turbine unit-1 and the turbine unit-2, respectively, for controlling the volumetric discharge through the turbines. The input turbine valve signal for unit-1 is given by

$$u_{v1} = \begin{cases} 0.68 & 0 < t \leq 500\,\text{s} \\ \frac{0.68}{50}(t - 550) + 0.98 & 500\,\text{s} < t \leq 550\,\text{s} \\ 0.98 & 550\,\text{s} < t \leq 1200\,\text{s} \end{cases},$$

and the input turbine valve signal for unit-2 is given by,

$$u_{v2} = \begin{cases} 0.55 & 0 < t \leq 500\,\text{s} \\ \frac{0.55}{50}(t - 550) + 0.93 & 500\,\text{s} < t \leq 550\,\text{s} \\ 0.93 & 550\,\text{s} < t \leq 1200\,\text{s}. \end{cases}$$

For inputs u_{v1} and u_{v2}, the mechanical power outputs for the turbine unit-1 (Figure 5c) and the turbine unit-2 (Figure 5d), the turbines inlet pressure p_{tr} (Figure 5e), and the air pressure inside the surge tank p_c (Figure 5f) are recorded for 1200 s with the measurement samples taken at each second. The air pressure p_c is measured using the pressure sensor PARO scientific 8DP000-S with an error of less than 0.01% of full scale of 6 Mpa, the turbine inlet pressure p_{tr} is measured using the pressure sensor PARO scientific DIQ 73K with an error of less than 0.04% of full scale of 20 Mpa, and the measurements for the mechanical power outputs are provided by the plant owner from Torpa HPP. The information about Torpa HPP and its experimental procedures are taken from [24]. Figure 5 shows that the simulation corresponds well with the real measurements in the case of power productions from the turbines (Figure 5c,d). In the case of the turbine inlet pressure p_{tr} (Figure 5e) there is an steady-state error of 0.6 bar for $0 < t \leq 500$ s. We believe that the steady-state error in p_{tr} for $0 < t \leq 500$ s can be eradicated by the inclusion of detailed geometrical dimensions for the headrace tunnel. In this paper, the headrace tunnel is considerd with a simple slanted pipe geometry as shown in Figure 4a. Similar steady-state error can be seen in the case of the height of water level inside the ACST h (Figure 5g) with negligible error of 0.05 m. In the case of air pressure inside the ACST p_c, the simulation and the measurement data are in good agreement. The measurement sampling rate in the case of water level h, air pressure p_c, and turbine power outputs are slower and oscillatory because the data are only recorded after a minimum change in the measured value, which may be the reason for the steady-state errors and phase difference between the simulation and measurements shown in Figure 5c,d,f,g. In addition, in Figure 5f,g for $800\,\text{s} < t \leq 1200$ s, the simulated values have poorly damped oscillation while the measurement quickly reaches a steady value. The simulated and the experimental dynamics of the variables (p_c and h) are not captured well because of the slower and oscillatory sampling rate of the sensors. The simulation and the real measurements are matched by manual tuning of pipe roughness height of the headrace tunnel ($\varepsilon \approx 0.4$ mm), hydraulic diameter of the access tunnel $D_t \approx 15$ m, and hydraulic diameter of the air chamber $D \approx 24$ m.

Table 1. Parameters and operating conditions of the ACST for Torpa HPP.

Quantity	Symbol	Value
Hydraulic diameter of the throat	D_t	15 m
Hydraulic diameter of the chamber	D	24 m
Length of the throat	L_t	29 m
Total height	H	50 m
Total length	L	58 m
Pipe roughness height	ε	0.9 mm
Total volume	$-$	$17 \cdot 10^3$ m^3
Operating temperature	T°	293 K
Adiabatic exponent for air at STP	γ	1.4
Molar mass of air at STP	M_a	$29 \cdot 10^{-3}$ kg mol^{-1}
Universal gas constant	R	8.314 JK^{-1} mol^{-1}
Initial pressure of air	$p_c(0) = p_{c0}$	$41 \cdot 10^5$ Pa
Initial water level	$h(0) = h_{c0}$	27 m
Initial volume of air	V_0	$13 \cdot 10^3$ m^3

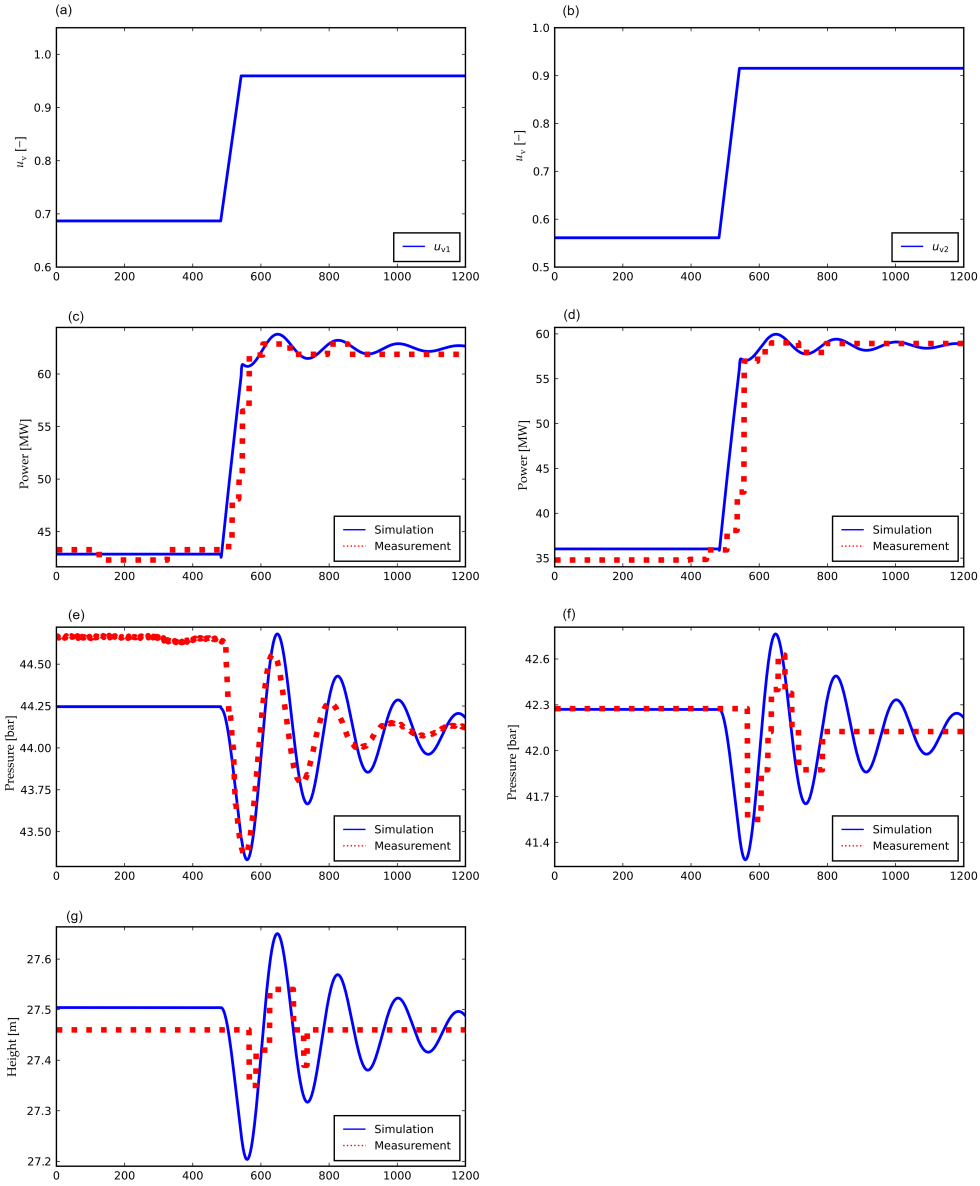

Figure 5. Simulation versus real measurements for Torpa HPP, (**a**) turbine valve signal for unit-1, (**b**) turbine valve signal for unit-2, (**c**) power output for unit-1, (**d**) power output for unit-2, (**e**) inlet pressure of the turbine units or the outlet pressure of the penstock, (**f**) air cushion pressure inside the ACST, and (**g**) height of water level inside the ACST.

3.2. Effect of Air Friction Inside ACST

We now consider Torpa HPP with each of the turbine units rated at 75 MW as a single entity, for simplification, with 150 MW with input u_v as the turbine valve signal. This simplification is made for studying the hydraulic behavior of the ACST in terms of the air friction inside the ACST, and the operation of Torpa HPP with respect to load acceptance and rejection (Section 3.3). Only simulated results will be presented in the sequel.

The air friction force $F_{D,a}$ modeled using Darcy's friction factor f_D inside the ACST of Torpa HPP is considered using Equation (12) for the case of water level $h \leq H_t$, and using Equation (19) for the case of water level $h > H_t$. The input to the turbine with valve signal u_v for the simulation purpose is given by

$$u_{\mathrm{v}} = \begin{cases} 0.5 & 0 < t \leq 500\,\mathrm{s} \\ 0.95 & 500\,\mathrm{s} < t \leq 1500\,\mathrm{s} \end{cases}$$

where the hydro-turbine is loaded from half-load to nominal load at time $t = 500\,\mathrm{s}$.

Figure 6 shows hydraulic behavior of the ACST for the turbine loading from 50% to 95%. Figure 6b–d show the water level h inside the ACST, the air cushion pressure p_{c}, and the inlet turbine pressure p_{tr}, respectively, for the ACST modeled with and without the air friction consideration. From Figure 6c, we see that the differences in air cushion pressure p_{c} for the ACST modeled with and without the air friction consideration is in the order of $10^{-5}\,\mathrm{bar} = 1\,\mathrm{Pa}$, even for the turbine loaded from half load to the nominal operation. This is because of the fact that fluid frictional force F_{f} depends on Darcy's friction factor f_{D}, and f_{D} depends on Reynolds' number $N_{\mathrm{Re}} = \frac{\rho|v|D}{\mu}$ where μ is the dynamic viscosity of the fluid. At STP, $\mu_{\mathrm{air}} = 1.81 \cdot 10^{-5}\,\mathrm{Pa \cdot s}$ and $\mu_{\mathrm{water}} = 8.90 \cdot 10^{-4}\,\mathrm{Pa \cdot s}$ which can be approximated as $\mu_{\mathrm{water}} \approx 100\,\mu_{\mathrm{air}}$.

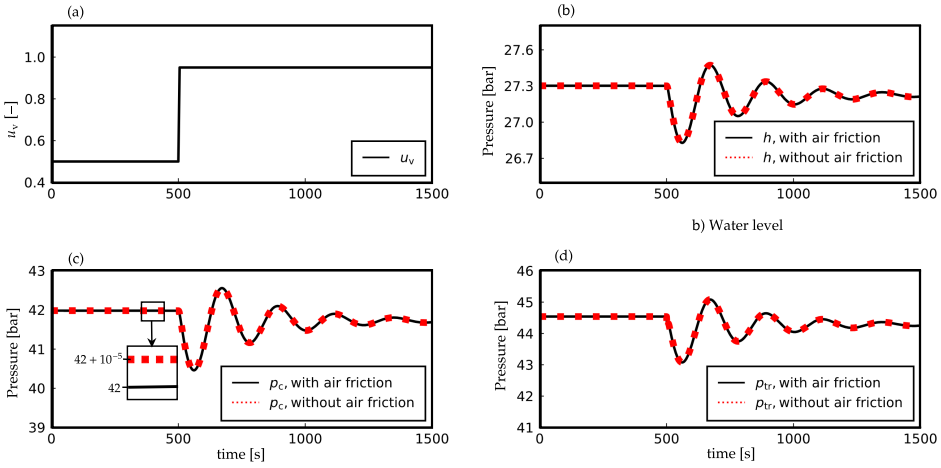

Figure 6. ACST model with and without frictional force due to the air inside ACST for Torpa HPP, (**a**) turbine valve signal u_{v}, (**b**) water level h inside ACST, (**c**) air cushion pressure p_{c}, and (**d**) turbine inlet pressure p_{tr}.

3.3. Operations of ACST in Load Acceptance and Rejection

Load acceptance and rejection are created by changing the turbine valve signal u_{v} from one operating condition to another operating condition, and are described in the sequel.

3.3.1. Load Acceptances

We consider Torpa HPP running at *no load* condition for a time period of 500 s. At $t = 500\,\mathrm{s}$, a different load acceptance condition is created by changing the turbine valve signal u_{v}, and the hydraulic behavior of the ACST is observed for the next 1500 s. The turbine valve signal u_{v} is generated as

$$u_{\mathrm{v}} = \begin{cases} 0 & 0 < t \leq 500\,\mathrm{s} \\ u_{\mathrm{va}} & 500\,\mathrm{s} < t \leq 2000\,\mathrm{s} \end{cases}$$

where $u_{\mathrm{va}} \in \{0.25, 0.5, 0.75, 1.0\}$ for load acceptances of 25%, 50%, 75%, and 100%, respectively. For a total load acceptance (TLA) the load acceptance is 100%.

3.3.2. Load Rejections

In contrast to the load acceptances, we now consider Torpa HPP running at *full load* condition for a time period of 500 s. At $t = 500\,\mathrm{s}$, a different load rejection condition is

created by changing the turbine valve signal u_v, and the hydraulic behavior of the ACST is observed for the next 1500 s. The turbine valve signal u_v is generated as

$$u_v = \begin{cases} 1.0 & 0 < t \leq 500\,\text{s} \\ u_{vr} & 500\,\text{s} < t \leq 2000\,\text{s} \end{cases}$$

where $u_{vr} \in \{0.75, 0.5, 0.25, 0.0\}$ for load rejections of 25%, 50%, 75%, and 100%, respectively. For a total load rejection (TLR), the load rejection is 100%.

Figure 7 shows hydraulic performance of the ACST during load acceptances and rejections for Torpa HPP. Figure 7a,c,e,g shows the turbine valve signal u_v, the air pressure p_c, the turbine inlet pressure p_{tr} and the water level inside ACST h, respectively, for the different percentage change in the load acceptances. Similarly, Figure 7b,d,f,h shows u_v, p_c, p_{tr} and h, respectively, for the different percentage change in the load rejections.

Figure 7a shows the turbine valve signal generated for load acceptances of 25%, 50%, 75%, and 100%. Figure 7c, at $t = 500$ s, shows that from the no load operation to TLA, the difference in the air pressure p_c inside the ACST is around 4 bar. Similarly, Figure 7e shows that the difference in turbine inlet pressure p_{tr} is around 3 bar, and Figure 7e shows that the difference in the water level h inside the ACST is around 1 m. In addition, Figure 7c shows that the difference in p_c from no load operation to 25% load acceptance, 50% load acceptance and 75% load acceptance are around 1 bar, 2 bar and 3 bar, respectively. Similarly, results can be obtained for p_{tr} (Figure 7e) and h (Figure 7g). For p_c, p_{tr} and h oscillation dies out as the time progresses for $t > 500$ s.

Figure 7b shows the turbine valve signal generated for load rejections of 25%, 50%, 75%, and 100%. Figure 7d, at $t = 500$ s, shows that from full load operation to TLR, the difference in p_c is around 4 bar as similar in the case of TLA. Similarly, the difference is around 3 bar in the case of p_{tr}, as shown in Figure 7f. The difference in h from full load operation to TLR is also 1 m, as in the case of TLA. Similarly, from Figure 7d, the difference in p_c from full load operation to load rejections of 25%, 50% and 75% are around 1 bar, 2 bar and 3 bar, respectively. Similar results can be obtained for p_{tr} (Figure 7f) and h (Figure 7h). For p_c, p_{tr} and h, oscillation dies out for $t > 500$ s, similar to the case of load acceptances. However, the oscillation dies out sooner in the case of TLA than TLR.

3.3.3. ACST as a Flexible Hydro Power

The results for Figure 7 show hydraulic behavior of the ACST in the case of load acceptance and rejection. The difference in the water level is around 1 m for both TLA and TLR. Similarly, the difference in the air pressure is around 4 bar for both TLA and TLR. Referring to the results on the hydraulic performance of the ACST from Section 3.3 and the study carried out for different types of open surge tanks in [6] clearly indicates that ACST has a robust performance on suppressing water mass oscillation and water hammer pressure during a higher percentage of load acceptances and rejections, unlike different types of open surge tanks. Since one of the prominent requirements of a flexible hydro power plant is to have a robust operation under various load acceptances and rejections, a hydro power plant operated with ACST makes it a potential candidate for participating in the concept of flexible hydro power.

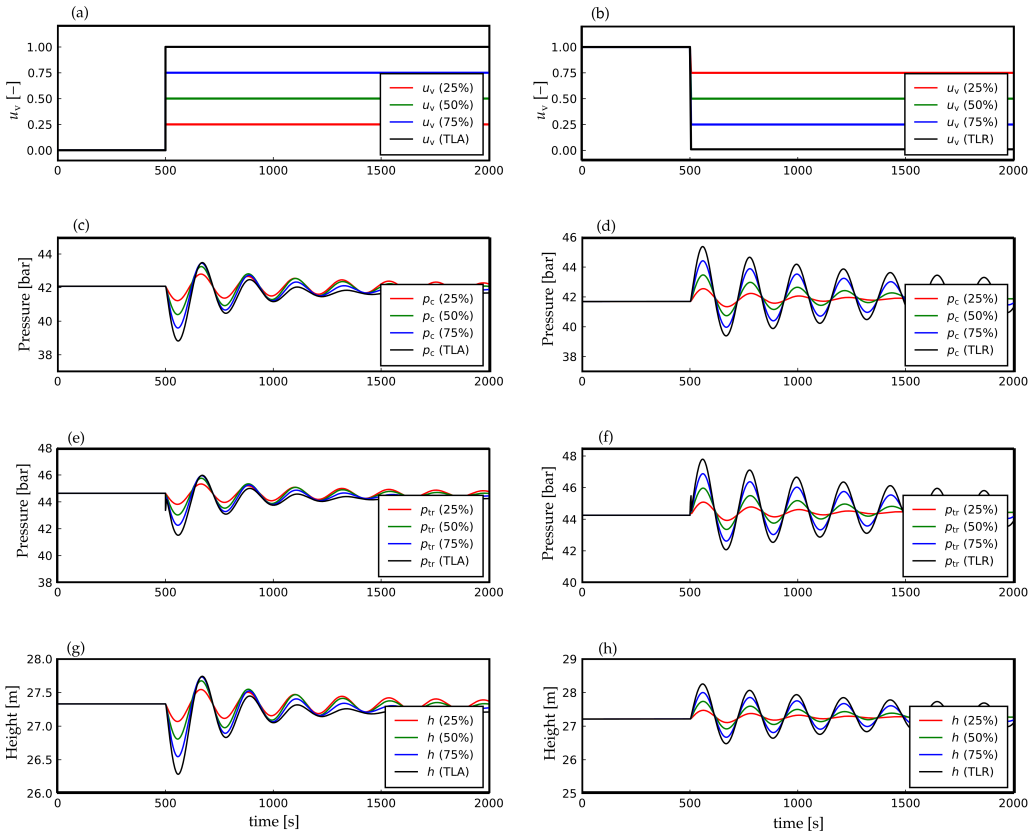

Figure 7. Hydraulic performance of the ACST for Torpa HPP for the different percentage change in the load acceptances and the load rejections, (**a**) turbine valve signal u_v as an input to the load acceptances, (**b**) turbine valve signal u_v as an input to the load rejections, (**c**) air pressure p_c for the load acceptances, (**d**) air pressure p_c for the load rejections, (**e**) turbine inlet pressure p_{tr} for the load acceptances, (**f**) turbine inlet pressure p_{tr} for the load rejections, (**g**) water level inside the ACST h for the load acceptances, and (**h**) water level inside the ACST for the load rejections.

4. Conclusions and Future Work

A mechanistic model of an ACST has been developed considering an access tunnel connected to an air chamber. The difference in diameters of the access tunnel and the air chamber has been taken into consideration. The model is further enhanced with the inclusion of Darcy's friction force for air inside the ACST. Model fitting is done for the 150 MW Torpa HPP. The experimental data and the model simulation were matched by manual tuning of pipe roughness height of the headrace tunnel, and hydraulic diameters of the access tunnel and the air chamber of the ACST. Apart from the model fitting, simulation results show that the effect of air friction inside the ACST is negligible as compared to water friction. The simulation studies carried out for load acceptance and rejection show the robust hydraulic behaviors of the ACST in terms of suppressing water mass oscillation and water hammer pressure, which indicate that a hydro power plant with ACST makes it a potential candidate for flexible hydro power in case of an energy-mix (intermittent and dispatchable sources) interconnected power grid.

Future work includes the study of the hydraulic behavior of ACST in interconnected grids supplied with intermittent generation. In addition, the model for ACST can be improved using Lagrangian computational fluid dynamics. For the Lagrangian approach, the meshless discretization technique smoothed particle hydrodynamics (SPH) can be used to handle coupling between the free water surface and air inside the ACST [25,26].

Author Contributions: Conceptualization, M.P., K.V., R.S. and B.L.; methodology, M.P., R.S. and B.L.; software, M.P. and D.W.; validation, M.P., K.V. and B.L.; formal analysis, M.P.; investigation, M.P.; resources, M.P., D.W. and K.V.; writing—original draft preparation, M.P.; writing—review and editing, M.P.; visualization, M.P. and B.L.; supervision, D.W., K.V. and B.L. All authors have read and agreed to the published version of the manuscript.

Funding: This research received no external funding.

Institutional Review Board Statement: Not applicable.

Informed Consent Statement: Not applicable.

Data Availability Statement: Not applicable.

Acknowledgments: Help and discussions with Liubomyr Vytvytsky, ABB Oslo, regarding model tuning is gratefully acknowledged.

Conflicts of Interest: The authors declare no conflict of interest.

References

1. Pandey, M.; Winkler, D.; Sharma, R.; Lie, B. Using MPC to Balance Intermittent Wind and Solar Power with Hydro Power in Microgrids. *Energies* **2021**, *14*, 874. [CrossRef]
2. Pandey, M.; Lie, B. The Role of Hydropower Simulation in Smart Energy Systems. In Proceedings of the 2020 IEEE 7th International Conference on Energy Smart Systems (ESS), Kyiv, Ukraine, 12–14 May 2020 ; pp. 392–397.
3. Charmasson, J.; Belsnes, M.; Andersen, O.; Eloranta, A.; Graabak, I.; Korpås, M.; Helland, I.; Sundt, H.; Wolfgang, O. *Roadmap for Large-Scale Balancing and Energy Storage from Norwegian Hydropower: Opportunities, Challanges and Needs until 2050*; SINTEF Energi AS: Trondheim, Norway, 2018.
4. Huertas-Hernando, D.; Farahmand, H.; Holttinen, H.; Kiviluoma, J.; Rinne, E.; Söder, L.; Milligan, M.; Ibanez, E.; Martínez, S.M.; Gomez-Lazaro, E.; et al. Hydro power flexibility for power systems with variable renewable energy sources: An IEA Task 25 collaboration. *Wiley Interdiscip. Rev. Energy Environ.* **2017**, *6*, e220. [CrossRef]
5. Graabak, I.; Korpås, M.; Jaehnert, S.; Belsnes, M. Balancing future variable wind and solar power production in Central-West Europe with Norwegian hydropower. *Energy* **2019**, *168*, 870–882. [CrossRef]
6. Pandey, M.; Lie, B. The influence of surge tanks on the water hammer effect at different hydro power discharge rates. In Proceedings of the SIMS 2020, Oulu, Finland, 22–24 September 2020; Linköping University Electronic Press: Linköping, Sweden, 2020; pp. 125–130.
7. Vereide, K.; Richter, W.; Zenz, G.; Lia, L. Surge Tank Research in Austria and Norway. *Wasserwirtschaft* **2015**, *1*, 58–62. [CrossRef]
8. Vereide, K.; Lia, L.; Nielsen, T. Physical modelling of hydropower waterway with air cushion surge chamber. In Proceedings of the 5th International Symposium on Hydraulic Structures, Brisbane, Australia, 25–27 June 2014.
9. Pandey, M.; Lie, B. Mechanistic modeling of different types of surge tanks and draft tubes for hydropower plants. In Proceedings of the SIMS 2020, Oulu, Finland, 22–24 September 2020; Linköping University Electronic Press: Linköping, Sweden, 2020; pp. 131–138.
10. Vereide, K.; Lia, L.; Nielsen, T.K. Hydraulic scale modelling and thermodynamics of mass oscillations in closed surge tanks. *J. Hydraul. Res.* **2015**, *53*, 519–524. [CrossRef]
11. Mosonyi, E. *Water Power Development: High-Head Power Plants*; Akadémiai kiadó: Budapest, Hungary, 1965; Volume 2.
12. Pickford, J. *Analysis of Water Surge*; Taylor & Francis: Abingdon, UK, 1969.
13. Jaeger, C. Present trends in surge tank design. *Proc. Inst. Mech. Eng.* **1954**, *168*, 91–124. [CrossRef]
14. Guo, J.; Woldeyesus, K.; Zhang, J.; Ju, X. Time evolution of water surface oscillations in surge tanks. *J. Hydraul. Res.* **2017**, *55*, 657–667. [CrossRef]
15. Lydersen, A. *Fluid Flow and Heat Transfer*; John Wiley & Sons Incorporated: Hoboken, NJ, USA, 1979.
16. Vereide, K.V. Hydraulics and Thermodynamics of Closed Surge Tanks for Hydropower Plants. Ph.D. Thesis, NTNU, Trondheim, Norway, 2016.
17. Wang, C.; Yang, J.; Nilsson, H. Simulation of water level fluctuations in a hydraulic system using a coupled liquid-gas model. *Water* **2015**, *7*, 4446–4476. [CrossRef]
18. Yulong, L. Studies on gas loss of air cushion surge chamber based on gas seepage theory. In Proceedings of the 2011 International Conference on Electric Technology and Civil Engineering (ICETCE), Lushan, China, 22–24 April 2011; pp. 723–725.
19. Ou, C.; Liu, D.; Li, L. Research on dynamic properties of long pipeline monitoring system of air cushion surge chamber. In Proceedings of the 2009 Asia-Pacific Power and Energy Engineering Conference, Wuhan, China, 27–31 March 2009; pp. 1–4.
20. Yang, X.L.; Kung, C.S. Stability of air-cushion surge tanks with throttling. *J. Hydraul. Res.* **1992**, *30*, 835–850. [CrossRef]
21. Vytvytskyi, L. *User's Guide for the Open Hydropower Library (OpenHPL)*; University of South-Eastern Norway, Porsgrunn, Norway, 2019.

22. Vytvytsky, L.; Lie, B. Comparison of elastic vs. inelastic penstock model using OpenModelica. In Proceedings of the 58th Conference on Simulation and Modelling (SIMS 58), Reykjavik, Iceland, 25–27 September 2017; Linköping University Electronic Press: Linköping, Sweden, 2017; Volume 138, pp. 20–28. [CrossRef]
23. Vytvytskyi, L.; Lie, B. Mechanistic model for Francis turbines in OpenModelica. *IFAC-PapersOnLine* **2018**, *51*, 103–108. [CrossRef]
24. Vereide, K.; Svingen, B.; Nielsen, T.K.; Lia, L. The effect of surge tank throttling on governor stability, power control, and hydraulic transients in hydropower plants. *IEEE Trans. Energy Convers.* **2016**, *32*, 91–98. [CrossRef]
25. Rakhsha, M.; Kees, C.E.; Negrut, D. Lagrangian vs. Eulerian: An analysis of two solution methods for free-surface flows and fluid solid interaction problems. *Fluids* **2021**, *6*, 460. [CrossRef]
26. Bimbato, A.M.; Alcântara Pereira, L.A.; Hirata, M.H. Study of surface roughness effect on a bluff body—The formation of asymmetric separation bubbles. *Energies* **2020**, *13*, 6094. [CrossRef]